HHS Public Access

Author manuscript

Magn Reson Med. Author manuscript; available in PMC 2015 November 01.

Published in final edited form as:

Magn Reson Med. 2015 November ; 74(5): 1397–1405. doi:10.1002/mrm.25521.

A Method for Safety Testing of Radiofrequency/Microwave-Emitting Devices Using MRI

Leeor Alon[1,2,3,4,*], **Gene Y. Cho**[1,2,4], **Xing Yang**, **Daniel K. Sodickson**[1,2,3], and **Cem M. Deniz**[1,2,3,4]

[1]The Bernard and Irene Schwartz Center for Biomedical Imaging, Department of Radiology, New York University, School of Medicine, New York, New York, USA

[2]Sackler Institute of Graduate Biomedical Sciences, New York University School of Medicine, New York, New York, USA

[3]NYU WIRELESS, Polytechnic Institute of New York University, Brooklyn, New York, USA

[4]RF Test Labs, Inc., New York, New York, USA

Abstract

Purpose—Strict regulations are imposed on the amount of radiofrequency (RF) energy that devices can emit to prevent excessive deposition of RF energy into the body. In this study, we investigated the application of MR temperature mapping and 10-g average specific absorption rate (SAR) computation for safety evaluation of RF-emitting devices.

Methods—Quantification of the RF power deposition was shown for an MRI-compatible dipole antenna and a non–MRI-compatible mobile phone via phantom temperature change measurements. Validation of the MR temperature mapping method was demonstrated by comparison with physical temperature measurements and electromagnetic field simulations. MR temperature measurements alongside physical property measurements were used to reconstruct 10-g average SAR.

Results—The maximum temperature change for a dipole antenna and the maximum 10-g average SAR were 1.83° C and 12.4 W/kg, respectively, for simulations and 1.73° C and 11.9 W/kg, respectively, for experiments. The difference between MR and probe thermometry was <0.15° C. The maximum temperature change and the maximum 10-g average SAR for a cell phone radiating at maximum output for 15 min was 1.7° C and 0.54 W/kg, respectively.

Conclusion—Information acquired using MR temperature mapping and thermal property measurements can assess RF/microwave safety with high resolution and fidelity.

Keywords

SAR; Local SAR; RF power deposition; RF Simulations; RF dosimetry; microwave dosimetry

[*]Correspondence to: Leeor Alon, Center for Biomedical Imaging, New York University School of Medicine, 660 First Avenue, Room 420, New York, NY 10016. leeor.alon@nyumc.org.

INTRODUCTION

During the last decade, there has been rapid development of wireless technology worldwide (1). The rising number of wireless device users has raised concern about the possible health effects of radiofrequency (RF)-transmitting devices, especially mobile phones (2). It is known that exposure to RF radiation results in increased heating of tissue via Joule and dielectric heating mechanisms (3,4). As specified by the Federal Communications Commission (FCC) and other regulatory bodies, the specific absorption rate (SAR) from RF-emitting devices must be measured prior to entering the consumer market in order to prevent the deposition of excessive RF energy into the body (5,6). SAR is the rate at which RF energy is absorbed in biological tissue and depends on several factors, including the antenna design, the output power of the wireless device, distance between the transmitting device and the body, and the morphological features and electrical property distributions of the body (7).

Electromagnetic (EM) field simulations are often used to characterize the interaction between an antenna and a load for safety assessment of the RF antennas. However, modeling of complex antenna-load structures to match realistic physical conditions using EM field simulations is not straightforward (8,9), and possible discrepancies between simulated and manufactured devices may reduce the accuracy of RF safety assessment (10). Although simulations can be used to evaluate the RF energy deposition from wireless devices (11), the majority of RF-emitting devices are tested using physical probes (12), defined in this paper as conventional SAR measurement systems. Experimental measurement of SAR utilizes electric (E) field probes (10) that are mechanically moved using an articulated robotic arm in a point-by-point, grid-like fashion in three-dimensional (3D) space inside a phantom filled with a liquid mimicking the electrical properties of human tissues. This process of moving a robotic arm to scan the E field inside the phantom can take more than 20 min to determine the point of maximum average SAR. Additionally, E field probes require calibration in order to preserve isotropy of the probe measurements, and measurement of E field components within a few millimeters of the surface is challenging due to the thickness of the probe and the interaction of the EM field with phantom edges (8,10).

In addition to the E field probe dosimetry systems, a temperature-based dosimetry system was proposed using an array of optical fiber thermal sensors positioned inside a phantom, showing good agreement with E field probe measurements (13). However, spatial resolution has been limited because of the large number of temperature probes that need to be positioned inside the phantom invasively.

Recently, it has been shown that MRI temperature mapping has been used to quantify RF energy deposition induced by MRI coils (operating at the Larmor frequency) (14–16) and other antennas (17,18), where both RF heating and temperature mapping were conducted inside the bore of the MRI scanner. However, many wireless devices are not MRI-compatible and therefore cannot be inserted inside the bore of the magnet while maintaining standard operation of the device.

In this study, we established a seminal framework for the use of MR technology for RF safety assessment of RF/microwave emitting devices that has not been rigorously investigated in prior studies. First, MRI temperature mapping is shown to be used for accurately mapping small temperature changes induced in a phantom, using RF/microwave exposure from devices driven with less than 1 W of power. Second, we demonstrated that MRI temperature mapping has the capability to characterize heating from wireless devices that are not necessarily MRI compatible. Finally, we computed the 10-g average SAR via inversion of the heat equation using high-resolution temperature mapping in combination with phantom thermal property measurements. The 10-g average SAR computation is demonstrated for both an MR-compatible dipole antenna and a non–MR-compatible Global System for Mobile Communications (GSM) cell phone.

THEORY

The heat equation with source term is a parabolic partial differential equation that captures the behavior of temperature in space and time when a body is exposed to an external energy source. The equation in nonperfused, homogeneous media is expressed as (19):

$$\rho C\frac{dT}{dt}=\nabla\cdot(k\nabla T)+SAR_{\rho}, \quad [1]$$

where ρ is the tissue density (in kilograms per cubic meter), *C* is the heat capacity (in Joules per kilogram per degree Celsius), *k* is the thermal conductivity (in Watts per meter per degree Celsius), and *SAR* is the Specific Absorption Rate (in Watts per kilogram). SAR, the driving force for temperature rise as result of Joule/dielectric heating mechanisms, is defined as:

$$SAR=\frac{\sigma|\mathrm{E}|^2}{2\rho}, \quad [2]$$

where **E** is the induced peak E field (in Volts per meter) inside the body and σ is the electrical conductivity (in siemens per meter). If the heating time (e.g., due to an external RF source) is short, thermal diffusion can be ignored and integration of Equation 1 with respect to time results in SAR that can be defined as:

$$SAR=C\frac{\Delta T}{\Delta t}, \quad [3]$$

where Δ*T* (in degrees Celsius) is the temperature change induced during time interval Δt (in seconds). However, keeping the duration of heating short requires sufficient device output RF power in order to minimize the heat diffusion by capturing the initial slope of the temperature increase and using Equation 3. In practice, the magnitude of the E field produced by an antenna is limited by the maximum power capabilities of the RF amplifiers, conductivity of the phantom and other factors. Because of these limiting factors, longer RF heating durations are often needed to induce temperature changes detectable using MRI. In

such cases, heat diffusion needs to be taken into account to avoid introducing major errors on safety assessment (20).

Temperature to SAR Inversion Using MR Thermometry

Proton resonance frequency (PRF) temperature change reconstruction using MRI relies on phase subtractions between two phase images acquired before and after RF/microwave heating. A linear relationship between temperature and phase change is shown in the equation (21):

$$\Delta T = \frac{\phi_2 - \phi_1}{\alpha \gamma B_0 T E}, \quad [4]$$

where Φ_1 and Φ_2 are the spatially dependent phases acquired from pre- and post-heating spoiled gradient echo (GRE) imaging sequences, respectively, γ is the gyromagnetic ratio of protons (~42.58 × 10^6 in Hertz per Tesla), TE is the echo time of the GRE sequence, B_0 is the main magnetic field strength (in Tesla), and a is the temperature dependency of the chemical shift (in parts per million per degrees Celsius).

In order to ensure RF safety regulations using SAR (6), ΔT obtained from MR thermometry measurements needs to be converted to spatial-average SAR. In temperature-based RF safety assessment methods, RF/microwave heating duration plays an important role in computing SAR, as SAR is no longer directly proportional to the temperature change for longer heating periods.

In this section, the inversion of the heat equation is explained concisely [see Alon et al. (22) for a more detailed description]. The inversion of the heat equation is used to overcome RF safety assessment errors associated with the heat diffusion. Using the finite difference approximation in space and time, the heat equation (Eq. 1) can be written in the polynomial form

$$T_N(\mathbf{r}) = (1+\mathbf{L})^{N-1} T_1(\mathbf{r}) + \sum_{i=0}^{N-2} (1+\mathbf{L})^i f(\mathbf{r}), \quad [5]$$

where ***f*(r)** is the source term defined as $f(\mathbf{r}) = \Delta t * SAR(\mathbf{r}) * C(\mathbf{r})^{-1}$ **r** is the spatial position, T_1 and T_N are the initial and final temperature of the sample, respectively, and Δ*t* is the time interval. **L** is a linear Laplace operator defined as

$\mathbf{L} = \frac{1}{\rho(\mathbf{r}) C(\mathbf{r})} \cdot \Delta t \cdot \nabla \cdot (k(\mathbf{r}) \nabla T(\mathbf{r}))$. Because all the terms in Equation 5, except f (r), are measurable quantities (*k* and *C* can be measured using a thermal probe, and $\Delta T = T_N - T_1$ using MRI), the solution to this problem can be written in a linear matrix notation. *f*, which can be sparsely represented, is calculated using the following l_1 norm weighted least-squares minimization, which has been shown to be robust with respect to noise for sparse representations (23):

$$argmin_f ||\mathbf{A}f - b||_2 + \lambda ||f||_1. \quad [6]$$

Here, $b = T_N - (1+\mathbf{L})^{N-1} T_1$, $\mathbf{A} = \sum_{i=0}^{N-2} (1+\mathbf{L})^i$, and λ is the regularization parameter. The minimization function shown in Equation 6, once solved, facilitates the computation of SAR from MR thermometry measurements (22).

METHODS

Simulation Technique

EM field simulations were performed on the dipole antenna - phantom setup shown in Figure 1B in order to obtain the SAR distribution induced by the dipole antenna inside the phantom. The commercial Microwave Studio software suite (CST, Framingham, Massachusetts, USA) using the finite integration technique (FIT) was used for simulations. The parameters used in the FIT calculations were as follows: 9.3 million mesh cells with edge lengths ranging from 0.4 to 11 mm, feeding with a voltage source operating at 1.96 GHz. Simulated EM fields were exported to 83 × 82 × 83 voxels with an isotropic cell size of 2.7 mm. A 5-mm separation between the phantom and the dipole antenna was used to simulate the physical setup in the scanner room. The net input power used was 0.65 W, which is equal to the output power of the dipole antenna measured in the scanner room under loaded conditions. The computed SAR distribution alongside the measured thermal properties of the phantom were fed into a finite-difference approximation based temperature simulator (24) to calculate the temperature change in the phantom following RF exposure from the dipole antenna (Eq. 1). The boundary conditions around the phantom in the thermal simulations were the room temperature at 21° Celsius. The acrylic former was incorporated into both EM field and temperature simulations and had the following thermal properties: density of 1180 kg/m^3, heat capacity of 1470 J/kg-K, and thermal conductivity of 0.2 W/m·° C.

Once the temperature change maps were obtained from temperature simulations, Gaussian noise with a mean of 0 and standard deviation of 0.05° C was injected onto the temperature difference maps. The injected noise statistics were measured from MR thermometry experiments when no heating was induced without an external RF exposure source. The temperature with noise maps were then used to invert the heat equation as specified in the theory section. For the inversion, $\lambda = 5$ was used as determined empirically in previous studies (22). Following inversion of the heat equation, 10-g average SAR was computed by interpolating the SAR maps to 1 mm^3 resolution. Temperature difference maps and original and reconstructed 10-g average SAR were plotted and juxtaposed for coronal, axial, and sagittal slices of interest. The maximum and normalized root mean square error between the input and reconstructed SAR was used to investigate the accuracy of the inversion process.

Dipole Antenna Setup and Power Measurement System

A cylindrical gelatin-based phantom was used for safety assessment of a dipole antenna and a Global System for Mobile Communications (GSM) mobile phone. The phantom was constructed using an acrylic former with a diameter of 10.2 cm, a height of 11 cm, and a

thickness of 3 mm, as show in Figure 1C. The dielectric properties of the phantom approximated the properties defined in IEEE Standard 1528-2003 (25) for 1.96 GHz RF frequency. The specific composition of the phantom was 54.4% sucrose (>99%; Sigma-Aldrich, St. Louis, Missouri, USA), 40.7% water (Sigma-Aldrich), and 4.9% gelatin (Kraft, Northfield, Illinois, USA) by weight. A dielectric probe was used to measure the conductivity and relative permittivity of the phantom (Agilent 85070E dielectric probe kit; Agilent Technologies, Santa Clara, California, USA), which were $\rho = 1.5$ siemens per meter and $\varepsilon_r = 36$, respectively, and emulating the electrical properties of the average human brain at 1.96 GHz. The thermal properties of the phantom were measured using a thermal property analyzer (KD2 Pro; Decagon Devices, Pullman, Washington, USA) yielding a density of 1272 kg/m^3, heat capacity of 3543 J/kg-K, and thermal conductivity of 0.457 W/m·°C. Measurements were performed by exposing the phantom to different power levels of RF energy and aligning the MR temperature measurements with measurements from fluoroptical temperature probe of ±0.1°C accuracy (Luxtron m3300 biomedical lab kit; Luxtron, Santa Clara, California, USA). Because the compounds used to create the phantom can affect the proton frequency shift coefficient, the phantom's sensitivity to temperature change had to be calibrated by placing the phantom with temperature probes inside an MR coil and pulsating a high SAR sequence while measuring the MR phase changes and probe temperature difference. This calibration has to take place once per phantom in order to represent the real temperature change induced in the phantom. In the case of the phantom used in this study, α was calibrated to 0.009 PPM/°C.

A half wavelength ($\lambda/2$) dipole antenna was constructed using a non-ferromagnetic 0.47-mm-diameter semirigid coaxial cable (Haverhill Cable and Manufacturing Corporation, Haverhill, Massachusetts, USA), and a 50-Ψ characteristic impedance coaxial balun was used to drive the dipole antenna at a frequency of 1.96 GHz. The dipole antenna (Fig. 1A) was matched for maximum efficiency with S11 < −15 dB. The antenna was connected to an RF transmitter placed outside the Faraday cage of the MRI scan room via a 10-m-long non-ferromagnetic low-loss RF cable with a 0.9-dB insertion loss at 1.96 GHz. The RF transmitter consisted of two stages of amplifiers. A TriQuint Semiconductor AH212 1-W high-linearity, high-gain, InGaP HBT Amplifier (TriQuint Semiconductor, Hillsboro, Oregon, USA) was used for the drive stage, and a TriQuint Semiconductor AH420 4-W high-linearity, InGaP HBT Amplifier was used for the final stage. A high-power directional coupler (778D; Agilent Technologies) was connected between the transmitter and the long non-ferromagnetic low-loss cable, to monitor the forward and reflected power from the coupling port and the isolation port. The total loss of the components between the amplifier output and the antenna input, including the directional coupler, cables, connectors, and coaxial balun (Fig. 2B) was 3.2 dB at 1.96 GHz. A network analyzer (E5070B; Agilent Technologies) located outside the MRI Faraday cage was used as the RF signal generator. During the RF heating period, the antenna was operated in continuous wave mode (CW) for 6 minutes and 30 seconds with a net output power of 0.65W (as in the simulations) measured using a power sensor (NRP-Z11; Rhode & Schwarz, Munich, Germany) connected to the directional coupler.

The dipole antenna was positioned inside the bore of the magnet and connected to a network analyzer confirming matching and tuning of the dipole was not altered relative to the bench test. Fluoroptical temperature probes were used to measure the RF heating produced by driving the dipole antenna, confirming that RF heating was identical for the bench test setup and the setup inside the magnet bore.

Dipole Antenna Experiments

Prior to the dipole antenna RF heating experiment, the phantom was positioned inside the MR scanner room for 24 hours, allowing the phantom to reach room temperature. After the phantom reached room temperature, RF heating produced by the dipole antenna was measured using a 3T MR scanner and head and neck coil (Siemens Medical Solutions, Erlangen, Germany) with 20 receive channels. A gel-oil phantom setup was used wherein cylindrical oil phantoms were placed around the phantom to estimate the non–heat-related main magnetic field drift (21). Airflow inside the magnet bore was turned off to prevent cooling down of the phantom by forced convection of air. Multislice, interleaved, spoiled GRE measurements of the phantom before and after a heating period of 6-min, 30-s were acquired with the following parameters: pulse repetition time (TR) = 244 ms; echo time (TE) = 17 ms; voxel dimension = 2.7 × 2.7 × 5 mm; number of slices = 11; and total acquisition time = 31 s. The PRF method (Eq. 4) was used to convert multislice, multicoil GRE phase measurements into a temperature difference map of the heating caused by the dipole antenna (21). The phase images were subtracted and a phase correction was applied using the oil phantoms as a phase reference. For the phase correction, a two-dimensional (2D) second-order polynomial fit was used to characterize the phase drift associated with the main magnetic field using the equation

$$Y = a_0 + a_1 x + a_2 y + a_3 x^2 + a_4 y^2 + a_5 xy, \quad [7]$$

where Y is the phase information provided by the oil phantoms and x and y are the coordinate in a rectangular grid. The a_i coefficients of the equation above were estimated via simple matrix inversion. Oil phantoms were used for reference since they have a conductivity of ~0.04 siemens per meter (at 128 MHz), which makes the heating of the oil negligible when exposed to RF energy. A temperature difference map was used to calculate the SAR by the inversion of the heat equation using Equation 6. The accuracy of the MR thermometry was assessed multiple times against fluoroptical temperature probe measurements. The location of the fluoroptical temperature probes was identified using a 3D high-resolution MR image of 1 × 1 × 1 mm^3 (Fig. 2A). The high-resolution image was registered with the MR phase image for precise comparison of the MR temperature and fluoroptical temperature measurements, and the results were plotted. Additionally, RF heating solely from the MRI pulse sequences was evaluated independently. MR thermometry measurements were acquired while the dipole antenna was not driven, thus no RF heating was induced by the dipole antenna, confirming that RF heating from the imaging sequences and its contribution to the overall temperature change was minimal relative to the heat induced by the 1.96 GHz antenna. The temperature difference maps acquired using MR thermometry alongside the measured thermal properties of the phantom and the acrylic

former (as in the simulations) were then used to invert the heat equation and compute the SAR as shown in the theory section. In the computation of the 10-g average SAR, the duration of heating alongside the lag time between image acquisition and cessation of heating was monitored during the experiment and included in the reconstruction.

Cell Phone Experiment

A specific anthropomorphic mannequin (SAM) phantom (SAM-V4.5; Speag, Zurich, Switzerland) (25), the gold standard for cell phone RF/microwave safety compliance testing, was used for the MRI cell phone experiments (Fig. 1D). The SAM phantom was filled with dielectric water-based gel with conductivity of 1.4 siemens per meter and relative permittivity of 40, in accordance with RF/microwave regulatory safety testing requirements at the 1900 MHz band (25). The thermal property of the gel was measured using a thermal property analyzer yielding a density of 1000 kg/m^3, heat capacity of 2940 J/kg-K, and thermal conductivity of 0.347 W/m·°C. The PRF shift of the gel was measured as 0.01 PPM/°C.

The RF heating experiment was performed using a 3T whole body scanner and a using the birdcage body coil (Siemens Medical Solutions). Four cylindrical oil phantoms were placed around the gel phantom to estimate non–heat-related main magnetic field drift. A multi-TE spoiled 3D GRE imaging sequence was used to image the phantom pre- and post- RF heating. The following sequence parameters were used: TR = 28 ms, matrix size = 64 × 64 × 22, voxel dimension = 5 × 5 × 5 mm^3, flip angle = 15 degrees and total acquisition time = 39 seconds. The phase images were subtracted and a phase correction was applied using the oil phantoms as described in the dipole antenna experiments. Between the imaging sequences, the phantom was withdrawn and positioned 165 cm away from the magnet bore. An LG 920CU (LG Electronics, Seoul, South Korea) cell phone was programmed to transmit at maximum power at the 1900 MHz GSM band using a CMW500 (Rhode & Schwarz) base station emulator. The mobile phone was placed on a phone holder and positioned adjacent (but not touching) the right cheek of the phantom (Fig. 1D). RF heating from the mobile phone was induced for 15 min. After the RF heating was conducted, the phone was removed and the table was retracted inside the magnet bore. Removal of the phone and movement of the table until the beginning of the scan took 25 s. The temperature difference maps alongside the measured thermal properties of the phantom were then used to invert the heat equation and compute the SAR using $\lambda = 5$ as determined in previous studies (22). The inversion took into account the cool-down period of the phantom cessation of RF heating and the beginning of the MRI sequence.

RESULTS

Dipole-Antenna Simulation and Experimental Results

Figure 2C shows temperature measurements inside the phantom acquired using three fluoroptic probes. The maximum heating captured from the probe measurements was 1.02°C (probe A) as a result of a 6-min, 30-s RF heating period (Fig. 2C, minutes 3 to 9.5). MR thermometry results show good agreement with the fluoroptical temperature measurement, as shown in Table 1.

The results of the dipole simulation and experimental power deposition are shown for coronal, axial, and sagittal slices of interest as depicted in Figure 3A. The first column of Figure 3B shows the noise-added temperature simulation results using the SAR map generated by the FIT simulation as an input to a finite-difference temperature simulator solving the heat equation (Eq. 1). The maximum temperature change over the phantom was 1.83° C. The second column shows 10-g average SAR that is directly computed from FIT simulations. The third column displays the reconstructed 10-g average SAR, which is computed from noise-added temperature change maps using the inverse heat equation framework. The maximum 10-g average SAR from FIT simulations and noise-added temperature change map reconstructions was 12.1 W/kg and 12.4 W/kg (2.4% difference), respectively. The normalized root mean square error between the two maps was 1.1%. The experimental temperature change and reconstructed 10-g average SAR are displayed in Figure 3C. The maximum experimental temperature change was 1.73°C (5.8% difference compared with the simulation) and the maximum reconstructed 10-g average SAR was 11.9 W/kg (4.2% difference compared with the simulation).

Figure 4 shows the validation of MR thermometry results against temperature probe measurements. Results are summarized in Figure 4 showing a maximum measurement mismatch in all experiments of <0.15° C, verifying the accuracy of the MR temperature mapping.

Mobile Phone Experimental Results

Temperature change resulting from the mobile phone heating was calculated using the PRF method. The results from the temperature change map alongside thermal property measurements were used to compute the 10-g average SAR resulting from the power deposition from a cell phone (Fig. 5). Figure 5B plots the reconstructed temperature change (row 1) and 10-g average SAR (row 2) for coronal, axial, and sagittal slices of interest. The slices of interest on the SAM phantom are illustrated in Figure 5A. It should be noted that the cool-down was included in the 10-g average SAR reconstruction in order to reduce the errors in the 10-g average SAR (see discussion). The maximum temperature change generated by the phone over the RF heating duration was 1.73°C in close proximity to the cell phone antenna, whereas the maximum 10-g average SAR was 0.54 W/kg.

DISCUSSION

The results of this study demonstrate the use of MR imaging for safety quantification of RF/microwave emissions using the capability to map small temperature changes in a phantom. Moreover, this study illustrates that MR temperature-based RF safety evaluation can be used for safety and compliance evaluations of wireless devices such as cell phones, which are not necessarily MRI-compatible. Inversion of the heat equation was introduced and computation of the 10-g average SAR was conducted as required by regulatory bodies, such as the International Commission on Non-Ionizing Radiation Protection (6) and the FCC (26).

Alignment of simulated and experimental temperature change and 10-g average SAR are nontrivial, and significant care was taken to achieve such alignment. In practice, many conditions—including electrical conductivity, permittivity, tissue density, thermal

conduction, heat capacity, net power, precise length and orientation of the dipole, and heating and cool-down time—must be modeled accurately. Even though these factors have been modeled based on physical measurements, some discrepancy between simulated and experimental fields can occur. For example, slight geometrical inaccuracies, such as the angle of the dipole antenna next to the phantom, can cause discrepancies between simulated and experimental fields. Due to this and similar reasons, alignment of simulated and experimental fields can be challenging (8,9). Figure 3 shows that the inverse heat equation framework was able to accurately compute the simulated 10-g average SAR both in distribution and magnitude. Agreement has also been shown between the experimental and simulated temperature change and the reconstructed 10-g average SAR.

When simulating physical experiments, heat convection can have an effect on the resulting temperature distribution and reconstructed SAR distribution, especially when heating durations are long. In the experimental setup, the fan in the scanner room was turned off and a phantom shell was used to reduce any convection that may happen next to the phantom. Therefore, movement of air close to the phantom during heating is assumed to be minimal, and energy exchange due to air convection with the gel is small. The boundary conditions were validated when comparing the simulated and experimental dipole temperature difference maps. These maps show high correlation that would not be possible if convection had a large contribution to the cool down of the phantom.

The preliminary results on mapping of RF power deposition for a mobile phone are presented in Figure 5. The mobile phone was not MRI-compatible, and therefore, it was important to show for the first time that temperature change and 10-g average SAR can be reconstructed while RF/microwave heating was initiated outside the magnet bore. The capability to estimate RF power deposition that was induced outside the magnet bore potentially enables the evaluation of RF power deposition from a wide array of wireless devices. The measured maximum 10-g average SAR for the experimental setup was 0.54 W/kg using the maximum output power of the commercial cell phone. This resulted in SAR values that are compliant with the international safety limits of 2 W/kg. The capability to measure 0.54 W/kg of power deposited is most likely not a lower bound for the sensitivity of the measurement. Because the measurement is based on MR temperature measurements, improvement in the accuracy and sensitivity of the MR thermometry tools will enable computation of smaller SAR values. The lower bound of the dynamic range given in terms of temperature increase and heating time for which accurate SAR can be determined needs to be investigated in future studies.

In conventional SAR measurement systems, a robotic arm moves an E field probe in a grid-like fashion requiring a long time to acquire high-resolution SAR maps (on the order of 20 min). Lengthy acquisition time of current SAR measurement systems results in both limited sampling resolution (~$7 \times 7 \times 7$ mm^3 and ~$5 \times 5 \times 5$ mm^3 depending on an “area” or “zoom” scan) and limited number of sampled points (~250) (26,27). In order to achieve higher resolutions for capturing the maximum SAR, standardized extrapolation and interpolation techniques are employed (25). Using this MR-based methodology, probing closer to the surface temperature was feasible, and no extrapolation and interpolation techniques were required. Because temperature probing was conducted close to the surface

with better fidelity, computed 10-g average SAR was higher than the value of 0.39 W/kg reported to the FCC (27). The ratio of the conventional SAR measurement system to that of the MR-based computation of 10-g average SAR was 0.72.

In addition to inefficiencies on the speed and resolution, SAR measurement probes are designed to measure the E field isotropically, and large errors result at inhomogeneous regions such as at the phantom gel and air/shell boundary. With regard to the MR-based measurements, the sampling resolution is higher and k-space sampling (since there are no mechanically moving parts) is much faster relative to current SAR measurement systems; however, limitations can arise at boundary regions, especially when long TEs are employed due to magnetic susceptibility. At these regions, signal dephasing can reduce the capability of accurately measuring temperature change due to limited signal-to-noise ratio (SNR). For simple geometries such as a head or cylinder (as used in this study), off-resonance effects can be mitigated relatively easily using conventional B_0 shimming techniques. When scanning more elaborate phantom geometries with different magnetic/dielectric properties, shimming may be more difficult and validation may be required to prove there is sufficient SNR in the acquired image.

In the present study, the resolution was set based on SNR measurements in the preliminary experiments and knowledge of the expected radiation pattern at the designated frequency. For the given phantom and radiation source at 1.96 GHz, the penetration depth was calculated to be roughly 2.5 cm. We decided to use at least five sample points along the penetration depth distance (resolution ≤5 mm in any direction) to characterize the power deposition for the given RF heating period. Additionally, when computing 10-g average SAR, a larger averaging volume is taken. This blurring is significantly larger than partial volume effects that may happen due to temperature gradients throughout a voxel. It should be noted that most likely finer voxel sizes/longer RF heating periods might be required when assessing power deposition for the safety assessment of antennas operating at higher microwave frequencies, such as fifth-generation (5G) wireless devices, in which the penetration depth is smaller (28). Evaluation of these high-frequency microwave devices is an area of active research, and the use of MR for the purpose of testing 5G devices remains to be tested.

The SNR of temperature-related phase difference maps is directly proportional to the signal amplitude (21). Because this study was conducted on a phantom, a wide variety of single- and multichannel MR coils can provide high SNR for the temperature measurement, enabling the detection of small temperature changes. In the experimental setup, for both the dipole and the cell phone, the SNR was >120. Fabrication of a phantom with long T_2^* is desirable, as longer TEs are beneficial for observing small frequency shifts resulting in a finer temperature change resolution. Special attention was given to minimize the presence of bubbles in the gelatin phantom for minimizing the main magnetic field susceptibility inside the phantom. In order to optimize the pulse sequence parameter, the TE of the sequence must be close to the T_2^* of the phantom, thereby maximizing the sensitivity of the temperature measurement. Challenges inherent in the proposed technique include compensation for non– heat-related B_0 field changes that depend on the magnet, field of view, shim, sequences, shape of the scanned object, and other factors. These B_0 field

instabilities can be mitigated using oil phantoms positioned around the object being scanned combined with a 2D field extrapolation technique (29). Because the resonant frequency of oil changes by a negligible amount with heating, non– temperature-related magnetic field variations that resulted in a phase change between the pre- and post-RF heating were mapped using these phantoms. Additionally, other metabolites can be added to the phantom to provide a frequency reference (30), which will remove the requirement of external oil phantoms for reference.

It should be noted that the time between the cessation of RF/microwave heating and the beginning of the scan (i.e., the cool-down period) could introduce errors in direct average SAR calculations. These errors would be most pronounced at the tissue–air boundary, where air can cool down the phantom due to the Laplacian term in the heat equation. These errors are expected to increase as a function of the cool-down period. Previous studies have shown that during a 6-min heating period, underestimation of 10-g average SAR can be as much as 53% (20). These SAR estimation errors have been a motivation for using the heat equation inversion framework, which is based on physical measurements, acquired using MR and thermal property probes as well as the knowledge of spatio-temporal model of the nonperfused heat evolution. It has been shown that the utilization of the heat equation inversion was able to mitigate errors associated with heat diffusion and energy exchange with air (20).

Regulatory safety requirements at frequencies between 100 MHz and 6 GHz are currently based on average SAR calculations performed on homogeneous phantoms (25). These standards are valid for body-worn devices or devices used close to the body, which have highest power loss densities, and consequently, the maximum SAR is in superficial tissues. For these devices, homogeneous phantoms give a valid approximation for the maximum local SAR in the heterogeneous tissue distribution of the human body; however, it is not generally accepted that homogeneous phantoms are suitable for generalized assessment of RF/microwave. For example, if the hotspot of an antenna array is located in the gray matter of the brain, a heterogeneous, body-simulating phantom with gray matter–simulating tissue at the hotspot location rather than a homogeneous phantom would most likely be needed for proper RF/microwave safety assessment. Conventional SAR measurement systems are only capable of measuring power deposition in single-compartment homogenous phantoms. As a result, EM field simulations are used as an alternative to investigate power deposition on complex anatomical structures. Nonetheless, even when meticulous care is put into modeling the antenna setup in silico, accurate alignment of simulations and experimental settings for complex antenna setups is still an active area of research.

This study focused on demonstrating the use of accurate and high-resolution temperature mapping for assessing RF/microwave safety on homogeneous phantoms; however, it is important to mention that if information regarding the electrical tissue properties of the object being imaged can be obtained, this technique may not necessarily be limited to homogeneous phantoms, and the inverse problem can potentially be solved for heterogeneous objects.

CONCLUSION

We have presented a novel MRI-based method for wireless device safety evaluation in a dipole antenna and a commercial mobile phone. The measurement method is robust for imaging small temperature changes and computing average SAR in phantoms using MR acquisition with millimeter resolution. Our results showed excellent reproducibility and agreement with simulation and temperature probe measurements.

ACKNOWLEDGMENTS

We thank Christopher M. Collins and Yudong Zhu for input on EM field simulations and MR thermometry, Ricardo Otazo for help with L1 norm minimization, Theodore S. Rappaport for technical support on the wireless communication systems, and Leslie F. Greengard for contributions to the inverse heat equation framework.

REFERENCES

1. United Nations International Telecommunications Union. ICT facts and figures. International Telecommunications Union; Geneva, Switzerland: 2011.
2. World Health Organization. Research agenda for radio frequency fields. World Health Organization; Geneva, Switzerland: 2006.
3. Hrnjak M. Biological effects of radiofrequency irradiation and directions of further research. Vojnosanit Pregl. 1998; 55:79–85. [in Serbian]. [PubMed: 9612130]
4. Juutilainen J, de Seze R. Biological effects of amplitude-modulated radiofrequency radiation. Scand J Work Environ Health. 1998; 24:245–254. [PubMed: 9754855]
5. Council of the European Union. On the limitation of exposure of the general public to electromagnetic fields (0 Hz to 300 GHz). J Eur Communities. 1999; 1991999:59–70.
6. International Commission on Non-Ionizing Radiation Protection. Statement on the “Guidelines for limiting exposure to time-varying electric, magnetic, and electromagnetic fields (up to 300 GHz). Report #1538-5159 (Electronic) 0017–9078 (Linking); September 2009.
7. Christ A, Gosselin MC, Christopoulou M, Kuhn S, Kuster N. Age-dependent tissue-specific exposure of cell phone users. Phys Med Biol. 2010; 55:1767–1783. [PubMed: 20208098]
8. Brishoual M, Dale C, Wiart J, Citerne J. Methodology to interpolate and extrapolate SAR measurements in a volume in dosimetric experiment. IEEE T Electromagn C. 2001; 43:382–389.
9. Chavannes N, Tay R, Nikoloski N, Kuster N. Suitability of FDTD-based TCAD tools for RF design of mobile phones. IEEE Antenn Propag M. 2003; 45:52–66.
10. Schmid T, Egger O, Kuster N. Automated E-field scanning system for dosimetric assessments. IEEE T Microw Theory. 1996; 44:105–113.
11. Bit-Babik G, Guy AW, Chou CK, Faraone A, Kanda M, Gessner A, Wang J, Fujiwara O. Simulation of exposure and SAR estimation for adult and child heads exposed to radiofrequency energy from portable communication devices. Radiation research. 2005; 163:580–590. [PubMed: 15850420]
12. Institute of Electrical and Electronics Engineers. Recommended practice for determining the peak spatial-average specific absorption rate (SAR) in the human head from wireless communications devices: measurement techniques. IEEE Standard 1528-2013. 2013 (Revision of IEEE Standard 1528–2003).
13. Okano Y, Shimoji H. Comparison measurement for specific absorption rate with physically different procedure. IEEE Trans Instrum Meas. 2012; 61:439–446.
14. Deniz CM, Alon L, Brown R, Sodickson DK, Zhu Y. Specific absorption rate benefits of including measured electric field interactions in parallel excitation pulse design. Magn Reson Med. 2012; 67:164–174. [PubMed: 22135040]
15. Cline H, Mallozzi R, Li Z, McKinnon G, Barber W. Radiofrequency power deposition utilizing thermal imaging. Magn Reson Med. 2004; 51:1129–1137. [PubMed: 15170832]

16. Alon L, Deniz CM, Brown R, Sodickson DK, Zhu Y. Method for in situ characterization of radiofrequency heating in parallel transmit MRI. Magn Reson Med. 2013; 69:1457–1465. [PubMed: 22714806]
17. Gultekin DH, Moeller L. NMR imaging of cell phone radiation absorption in brain tissue. Proc Natl Acad Sci U S A. 2013; 110:58–63. [PubMed: 23248293]
18. Alon L, Cho GY, Yang X, Zhu Y, Sodickson DK, Deniz CM. RF-emission device safety testing using MRI. IEEE International Symposium on Antennas and Propogation and USNC-URSI National Radio Science Meeting. 2013 p 3747.
19. Feynman, RP.; Leighton, RB.; Sands, M. The Feynman lectures on physics. Vol. 3. Addison Wesley; Reading, MA: 1964.
20. Alon, L.; Cho, YG.; Sodickson, DK.; Deniz, CM. Calculation of 10g average SAR via inversion of the heat equation using MRI thermometry and thermal property measurements; In Proceedings of the 22nd Annual Meeting of ISMRM; Milan, Italy. 2014. Abstract 4902
21. Reike V, Pauly KB. MR thermometry. J Magn Reson Imaging. 2008; 27:376–390. [PubMed: 18219673]
22. Alon, L.; Cho, YG.; Sodickson, DK.; Deniz, CM. A non-electric (E) field based method for safety assessment of RF and microwave emitting devices; Paper presented at the 2014 Bioelectromagnetics Society Annual Meeting (Session 12–4); p 45
23. Candes EJ, Romberg JK, Tao T. Stable signal recovery from incomplete and inaccurate measurements. Commun Pur Appl Math. 2006; 59:1207–1223.
24. Collins CM, Liu W, Wang J, Gruetter R, Vaughan JT, Ugurbil K, Smith MB. Temperature and SAR calculations for a human head within volume and surface coils at 64 and 300 MHz. J Magn Reson Imaging. 2004; 19:650–656. [PubMed: 15112317]
25. Institute of Electrical and Electronics Engineers. IEEE recommended practice for determining the peak spatial-average specific absorption rate (SAR) in the human head from wireless communications devices: measurement techniques. IEEE Standard 1528-2003.
26. Federal Communications Commission. Mobile and portable devices RF exposure procedures. General RF exposure guidance. 2013 Technical Report.
27. Federal Communications Commission. LG920CU public test documentation. RF exposure testing. 2007. https://apps.fcc.gov/oetcf/eas/reports/ViewExhibitReport.cfm?mode=Exhibits&RequestTimeout=500&calledFromFrame=N&application_id=589543&fcc_id=BEJCU920. Accessed August 24, 2014
28. Kumar Mohapatra, S.; Ranjan Swain, B.; Pati, N.; Pradhan, A. Road towards mili meter wave communication for 5G network: a technological overview. Transactions on Machine Learning and Artificial Intelligence. 2014. doi: http://dx.doi.org/10.14738/tmlai.23.256
29. Rieke V, Vigen KK, Sommer G, Daniel BL, Pauly JM, Butts K. Referenceless PRF shift thermometry. Magn Reson Med. 2004; 51:1223–1231. [PubMed: 15170843]
30. Hekmatyar SK, Hopewell P, Pakin SK, Babsky A, Bansal N. Noninvasive MR thermometry using paramagnetic lanthanide complexes of 1,4,7,10-tetraazacyclodoecane-alpha,alpha′,alpha″,alpha‴-tetramethyl-1,4,7,10-tetraacetic acid (DOTMA4-). Magn Reson Med. 2005; 53:294–303. [PubMed: 15678553]

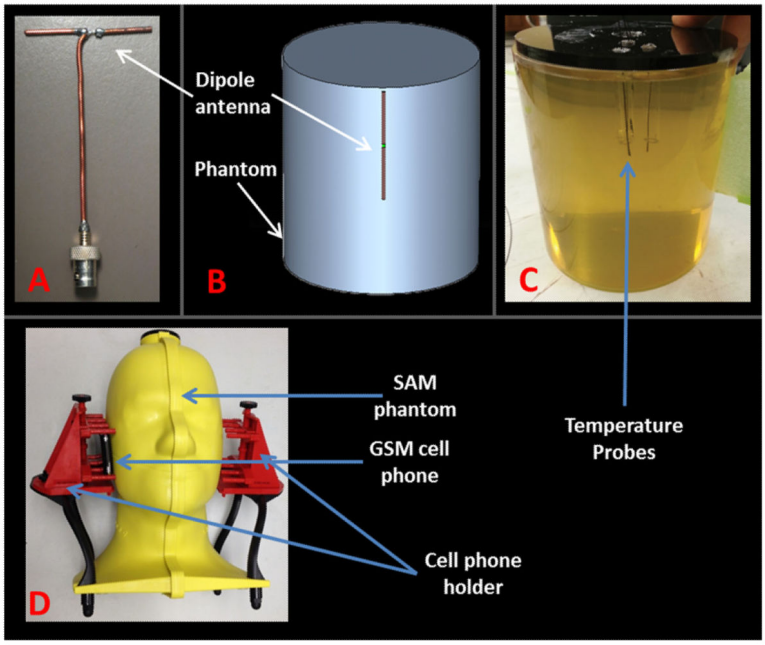

FIG. 1.

Experimental setup and configuration of numerical simulations. **A:** Dipole antenna with $\lambda/2$ length. **B:** FIT simulation setup of the dipole antenna and the gelatin phantom. **C:** Gelatin phantom and fluoroptic temperature probes. **D:** SAM head phantom, phone holder, and GSM phone setup used in the cell phone experiment.

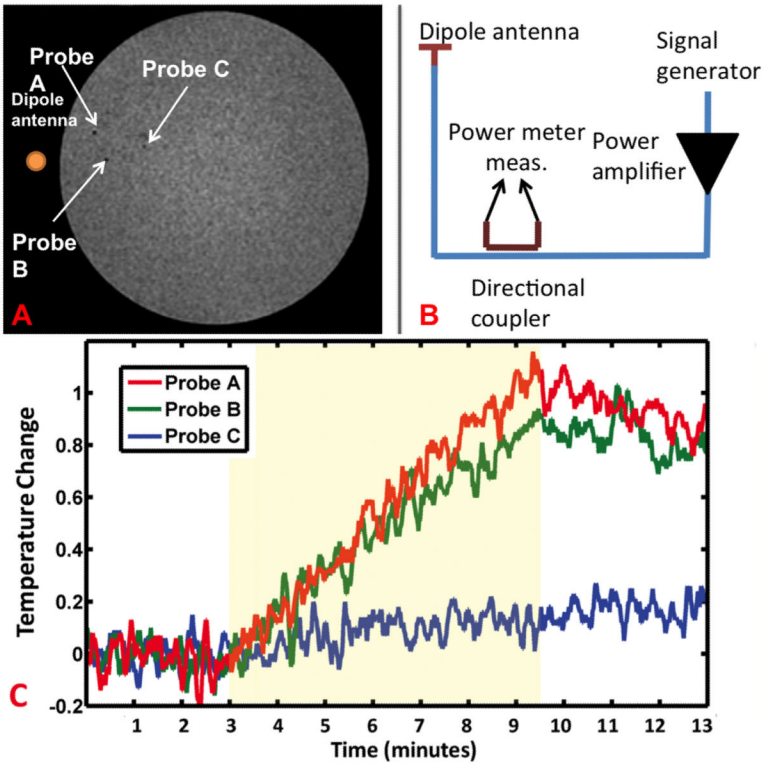

FIG. 2.

Fluoroptic temperature probe locations and temperature measurements. **A:** Locations of the fluoroptic probes within the phantom. **B:** Setup of dipole antenna circuit. **C:** Fluoroptic probe temperature measurements of dipole antenna heating. Heating occurred between minute 3 and minute 9.5 (highlighted in yellow).

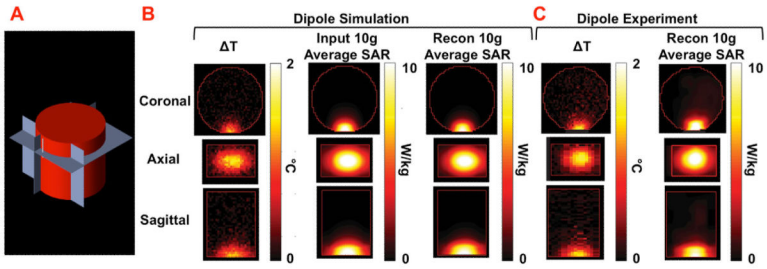

FIG. 3.

A: Illustration of the dipole setup. The different imaging slices of interest are shown in gray. **B:** Simulated temperature change (column 1), 10-g average SAR (column 2), and reconstructed 10-g average SAR (column 3). **C:** Experimentally measured temperature change and reconstructed 10-g average SAR for a dipole antenna.

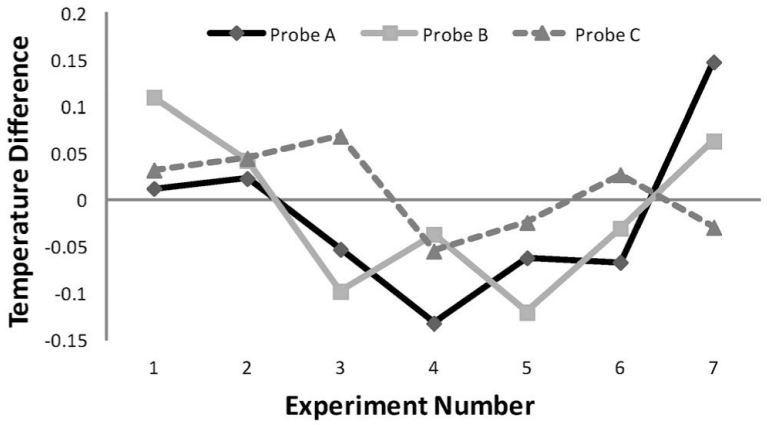

FIG. 4.

Error of MR thermometry measurements compared with fluoroptic temperature probe measurements from probes A–C in different experiments.

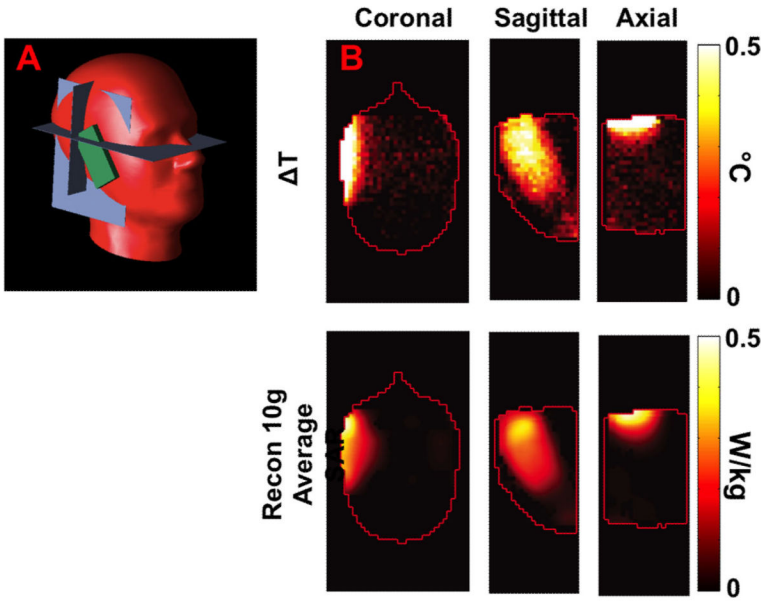

FIG. 5.

A: Illustration of the SAM phantom used in the cell phone experiment. Coronal, sagittal, and axial slices of interest are highlighted in gray. **B:** Maps of temperature change (top) and reconstructed 10-g average SAR (bottom).

Table 1

Dipole Antenna Experiment

Probe	Measured ΔT	MR thermometry	Error[a]
A	1.020°	1.003°	0.017°
B	0.870°	0.863°	0.007°
C	0.150°	0.179°	0.029°

[a]The absolute difference between MR thermometry and fluoroptic probe temperature measurements.